High-Resolution Solution Structure of the Beryllofluoride-Activated NtrC Receiver Domain[†]

Curtis A. Hastings,[‡,§] Seok-Yong Lee,[‡,ǁ] Ho S. Cho,[‡] Dalai Yan,[⊥,@] Sydney Kustu,[⊥] and David E. Wemmer*,[‡,ǁ,#]

Physical Biosciences Division, Lawrence Berkeley National Laboratory, 1 Cyclotron Road, Berkeley, California 94720, Graduate Group in Biophysics, University of California, Berkeley, California 94720, Department of Plant and Microbial Biology, University of California, 111 Koshland Hall, Berkeley, California 94720, and Department of Chemistry, University of California, B84A Hildebrand Hall, Berkeley, California 94720

ABSTRACT: Bacterial receiver domains mediate the cellular response to environmental changes through conformational changes induced by phosphorylation of a conserved aspartate residue. While the structures of several activated receiver domains have recently been determined, there is substantial variation in the conformational changes occurring upon activation. Here we present the high-resolution structure of the activated NtrC receiver domain (BeF_3^-−NtrC^r complex) determined using NMR data, including residual dipolar couplings, yielding a family of structures with a backbone rmsd of 0.57 ± 0.08 Å, which is compared with the previous lower-resolution structure of the phosphorylated protein. Both phosphorylation and beryllofluoride addition induce a shift in register and an axial rotation of α-helix 4. In this high-resolution structure, we are able to observe a concerted change in the positions of Thr82 and Tyr101; this correlated change in two conserved residues (termed Y−T coupling) has been considered a general feature of the conformational change in receiver domains upon activation. In NtrC, this correlated side chain shift, leading to the helix reorientation, is distinctly different from the smaller reorganization seen in other activated receiver domains, and involves numerous other residues which do not participate in conformational changes seen in the other systems. Titration of the activated receiver domain with peptides from the NtrC ATPase domain provides direct evidence for interactions on the rearranged face of the receiver domain, which are likely to be responsible for enabling assembly into the active aggregate. Analysis of the active structure also suggests that His84 may play a role in controlling the phosphate hydrolysis rate.

Protein phosphorylation is a common mechanism by which organisms effect signal transduction and metabolic regulation. In bacteria, "two-component" systems are the dominant mechanisms for responding to external stimuli. These systems use phosphotransfer between two conserved proteins, a histidine kinase and a response regulator, to propagate the signal (reviewed in ref *1*). Response regulators are often composed of a conserved N-terminal receiver domain, which becomes phosphorylated, and C-terminal effector domain-(s) whose activity is modulated by the receiver domain. Under appropriate environmental conditions, the histidine kinase becomes activated and phophorylates a conserved aspartate in the receiver domain. The phosphorylated receiver domain may act either positively (binding directly to another protein or domain to affect output) or negatively (relieving inhibition by weakened or altered binding to another domain). Nitrogen regulatory protein C (NtrC) in enteric bacteria plays a central role in the control of genes involved in nitrogen metabolism. It is composed of three domains: an N-terminal receiver domain, a central ATPase domain, and a C-terminal DNA binding domain. It is phosphorylated by the kinase NtrB, whose activity is ultimately regulated by the ratio of α-ketoglutarate to glutamine in the cell. Phosphorylation of the NtrC receiver domain (P-NtrC^r)[1] activates transcription by stimulating oligomerization and subsequently ATP hydrolysis, leading to an opening of the DNA at the transcription initiation site of the σ^{54}-polymerase-bound promoter (*2−4*).

* To whom correspondence should be addressed. Telephone: (510) 486-4318. Fax: (510) 486-6059. E-mail: dewemmer@lbl.gov.

[‡] Lawrence Berkeley National Laboratory.

[§] Current address: Institute for Physical Sciences, 1365 Beverly Rd., Suite 300, McLean, VA 22101.

[ǁ] Graduate Group in Biophysics, University of California.

[⊥] Department of Plant and Microbial Biology, University of California.

[@] Current address: Cumbre, Inc., 1502 Viceroy Dr., Dallas, TX 75235.

[#] Department of Chemistry, University of California.

[1] Abbreviations: NMR, nuclear magnetic resonance; rmsd, root-mean-square deviation; NOE, nuclear Overhauser effect; HSQC, heteronuclear single-quantum coherence; TSP, trimethylsilylproprionate; TPPI, time-proportional phase incrementation; NHCA, amide-H amide-N α-C correlation experiment; CBCA(CO)NH, β-C, α-C through carbonyl amide-N amide-H correlation experiment; TOCSY, total coherence spectroscopy; IPAP, in-phase/antiphase; NtrC^r, receiver domain of nitrogen regulatory protein C.

Structure determinations of stable phosphoproteins have provided insights into the structural basis for activation of proteins phosphorylated on tyrosine or serine/threonine (*5*– *9*). However, the active states of receiver domains have short half-lives, ranging from seconds to hours because of their own autophosphatase activity and the intrinsically labile aspartyl phosphate bond (*10*–*14*). This makes structural studies of receiver domains in their active state difficult. Despite this, several structures of phosphorylated receiver domains have recently been determined using different approaches to catch the active state. The receiver domain of Spo0A (P-Spo0A^r) from the hyperthermophile *Bacillus stearothermophilus* was unknowingly crystallized in the phosphorylated form following substitution of calcium for magnesium at the divalent cation site (*15*). The crystal structure of the phosphorylated receiver domain of FixJ (P-FixJ^r) was determined following demetalation (*16*), which inhibits dephosphorylation. The NMR structure of P-NtrC^r was determined using carbamyl phosphate to maintain a high steady state level of the protein in the phosphorylated state (*17*, *18*).

Recently, Yan *et al.* (*19*) discovered that beryllofluoride (BeF$_3^-$) forms a persistent complex with NtrC, fully activating the protein. Additional work showed that BeF$_3^-$ complexes with the response regulators CheY, OmpR, and NarL are functionally very similar to their phosphorylation-activated counterparts (*19*). The structure of beryllofluoride-activated CheY (BeF$_3^-$-CheY) was determined using NMR spectroscopy (*20*), and the crystal structures of both BeF$_3^-$-CheY and BeF$_3^-$-CheY complexed with the N-terminus of FliM, its downstream target, were determined (*21*, *22*). Comparison of the structures of FixJ, Spo0A, and CheY in their active states reveals a common conformational rearrangement involving coupled motion of two conserved residues in β-strand 4 (β4) and β5, Thr82 and Tyr101 (NtrC numbering is used throughout; the receiver domain corresponds to residues 1–124) which was termed Y–T coupling, and also a small displacement of α4 and reorganization of the loop between β4 and α4. The NMR structure of transiently phosphorylated NtrC^r displayed larger rearrangements of α3, β4, α4, and β5 (*17*). Helix 4 underwent a register shift and rotation about its long axis, resulting in a conformation similar to that observed in active CheY. In contrast, the conformations of α4 and the loops before and after α4 are significantly different in the inactive states of NtrC^r and CheY. The rotameric states and packing of Thr82 and Tyr101 were not well defined by the NMR data used to determine the structure of P-NtrC^r. Both inactive and active structures of DctD, more closely related to NtrC than the other receiver domains discussed above, have also been reported (*23*, *24*). As for FixJ, phosphorylation leads to a change in the dimerization interface.

To develop further insight into the structural changes that accompany NtrC^r activation, we determined a high-resolution structure of the stable BeF$_3^-$–NtrC^r complex using NMR spectroscopy. The three-dimensional (3D) NMR data yielded an ensemble of structures with a backbone rmsd of 0.57 ± 0.08 Å, and rather uniform backbone variation among the structures throughout the protein. In addition, we measured residual dipolar couplings for both P-NtrC^r and the BeF$_3^-$– NtrC^r complex. For P-NtrC^r, the agreement of these couplings with the previously determined structures of P-NtrC^r was

assessed to evaluate whether differences between the phospho and BeF$_3^-$-activated forms were real, or arose from a lack of definition of the phosphoprotein structure. Finally, we measured T_1, T_2, and heteronuclear NOE values for the backbone amides of the BeF$_3^-$–NtrC^r complex, and compared the order parameters obtained from a model-free analysis of the data with values for P-NtrC^r (*25*). The structural definition of the BeF$_3^-$-activated protein is significantly better than that of P-NtrC^r, allowing us to identify aspects of the structural changes that could not previously be seen.

To explore the interaction of NtrC^r with the central domain, titrations were done with a peptide containing residues 139– 160 of the central ATPase domain of NtrC [a region implicated in interaction with the receiver domain by Cys– EDTA–Fe cleavage studies (*26*) and EPR (*27*)]. Activation-dependent binding is expected if the peptide is involved in the interdomain contact, which should be reflected in chemical shift changes in that region.

MATERIALS AND METHODS

NMR Sample Preparation. Uniformly ^{15}N-labeled, uniformly ^{15}N- and ^{13}C-labeled, and 10% ^{13}C-labeled NtrC^r (residues 1–124 of NtrC) were prepared by growth on M9 minimal medium. The recombinant protein was expressed in *Escherichia coli* BL21(DE3)/pACYC cells and purified as described by Nohaile *et al.* (*28*). The purified protein was concentrated in an Amicon stirred cell concentrator with a 3 kDa cutoff membrane to a concentration of approximately 0.1 mM, dialyzed against 50 mM sodium phosphate (pH 6.75) and 50 mM NaCl, and concentrated in an Amicon "Centriprep" concentrator with a 3 kDa cutoff membrane to a final protein concentration of 1.1–1.5 mM. NMR samples were made 5% ^{2}H$_2$O, 4.4 mM BeCl$_2$, 7.2 mM MgCl$_2$, and 29 mM NaF. NMR samples of inactive NtrC^r were identical except for a lack of BeCl$_2$. Quantitative conversion to the beryllofluoride-bound state was verified by examination of the ^{15}N–^{1}H HSQC spectra. Peptides representing residues 134–160 (NGPTTDMIGEAPAMGDLFRIIGRLSRS) (27-mer), 139–160 (22-mer), and 143–160 (18-mer) of NtrC were prepared using standard Fmoc/HOBT-DCC chemistry on an automated synthesizer. Peptides were purified using reversed phase HPLC, and were verified by electrospray mass spectroscopy. A control peptide of the same sequence as residues 143–160 of NtrC but in reverse order (18-mer reverse) and a mutant peptide corresponding to residues 143–160 of NtrC S160F (18-mer S160F) were prepared identically. For all NMR experiments, peptide and NtrC^r were prepared as 2× stocks and combined. Sample concentrations were calculated assuming all counterions were trifluoroacetate and 10% of the dry weight was residual water. Following peptide dissolution, the pH of the sample was readjusted to 6.75 with 1 M NaOH.

NMR Spectroscopy. NMR data were acquired at 30 °C using a Bruker AMX-600 spectrometer equipped with a triple-resonance probe with triple-axis pulsed-field gradients, and a Bruker DRX-500 spectrometer equipped with a triple-resonance probe with single-axis pulsed-field gradients. Chemical shift values were externally referenced to TSP (^{1}H and ^{13}C) (*29*) and liquid ammonia (^{15}N) (*30*). Except where noted, indirect dimensions of multidimensional experiments

utilized the States−TPPI method for quadrature detection (*31*). Data were processed using Felix 97 (Molecular Simulations, Inc.). The data were apodized using skewed sine-bell functions. Linear prediction was used to increase the effective digital resolution in indirectly detected dimensions. Data were viewed and analyzed using the program NMRView (*32*).

Resonance Assignments and Constraint Generation. Nearly complete backbone and side chain resonance assignments were obtained through analysis of HNCA (*33*), CBCA(CO)-NH (*34*), ^{15}N-edited TOCSY-HSQC (*29*) and NOESY-HSQC (*35*), HCCH-TOCSY (*36*), and ^{13}C-edited HSQC-NOESY (*37*) spectra. Stereoassignments for nondegenerate leucine and valine residues were obtained from analysis of a ^{13}C−^{1}H HSQC spectrum of the BeF$_3$$^-$−NtrC^r complex grown on 10% [^{13}C$_6$]glucose. Resonances of the side chain carbon atoms of Ile55, Met60, Asp61, and Leu63 were initially identified from analysis of the four-dimensional (4D) ^{13}C- and ^{15}N-edited NOESY spectrum, and subsequently confirmed by analysis of the HCCH-TOCSY, ^{13}C-edited NOESY, and ^{15}N-edited NOESY spectra. Distance constraints were obtained from assigned cross-peaks in two-dimensional (2D) NOESY, 3D ^{15}N-edited NOESY-HSQC, 3D ^{13}C-edited HSQC-NOESY, 4D ^{13}C- and ^{15}N-edited HMQC-NOESY-HSQC, and 4D ^{13}C- and ^{13}C-edited HMQC-NOESY-HMQC (*38*) spectra. All NOESY spectra were collected with a mixing time of 100 ms. NOEs were categorized as strong, medium, or weak according to the peak intensities. Following correction for methyl groups, the strongest 25% of the peaks were categorized as strong, and the next strongest 25% were categorized as medium. Methyl group correction and bin limits were set using built-in functions of NMRView. The intensity of methyl NOEs was divided by 2, and the intensity of methyl−methyl NOEs was divided by 4 prior to binning. Corresponding initial upper distance limits for strong, medium, and weak NOEs were 2.8, 3.4, and 5.0 Å, respectively. Backbone torsion angle constraints were obtained from observed chemical shifts using the program TALOS, and were included in the structure calculations only where the $^3J_{HN-HA}$ value predicted from the TALOS-derived ϕ angle constraint agreed within 2 Hz with the value observed in a 3D HNHA spectrum. Where the TALOS-derived ϕ angle constraint did not agree with the observed $^3J_{HN-HA}$ value, the $^3J_{HN-HA}$ value was included in the structure calculations as a coupling constant constraint. χ^1 angle constraints for valine, threonine, and isoleucine and χ^2 angle constraints for leucine residues were obtained from long-range $J_{CC'}$ and $J_{NC'}$ experiments (*39*). Orientational constraints for ^{15}N−^{1}H bond vectors were obtained by comparison of IPAP-HSQC (*40*) spectra of an unaligned sample and a sample aligned using 30 mg/mL phage pf1 (*41*). Amide protons that were resistant to deuterium exchange were identified by dissolving a lyophilized sample in 99.99% ^{2}H$_2$O (CIL) and measuring residual peak heights. Amide protons with exchange rates at least 10-fold slower than those predicted by SPHERE [http://www.fccc.edu/research/labs/roder/sphere (*42*)] under the sample conditions that were used were identified as potential hydrogen bond donors.

Structure Calculations. Initial rounds of structure calculation were performed with the program DYANA (*43*) using distance constraints derived from NOE cross-peaks in the ^{15}N-edited NOESY and ^{13}C-edited NOESY spectra, and

direct refinement against $^3J_{HNHA}$ coupling constants obtained from analysis of the 3D HNHA spectrum. The structure of inactive NtrC^r was used to reduce the number of possible assignments using a distance cutoff of 10 Å. Once the structures converged to a backbone rmsd of <1.1 Å, hydrogen bond constraints were added for clearly identifiable donor−acceptor pairs where the exchangeable proton possessed an exchange rate at least 10-fold slower than those predicted by the SPHERE server for the sample conditions that were employed. Additional rounds of NOESY cross-peak assignment using structures of the BeF$_3$$^-$−NtrC^r complex determined in the previous round of structure calculation to filter assignment possibilities allowed the unambiguous assignment of ∼90% of the identified cross-peaks in the ^{15}N-edited NOESY spectrum and ∼70% of the identified cross-peaks in the ^{13}C-edited NOESY spectrum. At this point, the loops between β3 and α3 and between α3 and α4 remained poorly defined because of a lack of constraints. Consequently, 4D ^{13}C- and ^{15}N-edited and 4D ^{13}C- and ^{13}C-edited NOESY spectra were collected and assigned. Additional rounds of iterative NOESY cross-peak assignment and structure calculation were performed with inclusion of constraints derived from these spectra, as well as ϕ and ψ torsion angle constraints derived from analysis of chemical shifts using the program TALOS (*44*). Good convergence was obtained for both α3 and α4, and unambiguous assignments were obtained for 92% of the identified cross-peaks in the ^{15}N-edited NOESY spectrum and 75% of the identified cross-peaks in the ^{13}C-edited NOESY spectrum and 4D NOESY spectra.

The program CNS (*45*) was used for the final rounds of structure calculation to incorporate ^{15}N−^{1}H residual dipolar coupling measurements. Simulated annealing was accomplished using the "anneal" command with all parameters set to their default values. Initially, only NOE distance constraints, torsion angle constraints, and coupling constant constraints were included in the structure calculations. Multiple rounds of structure calculation and refinement of the distance constraint list were performed. Simulated annealing was accomplished through a multistage protocol involving 1000 steps of high-temperature (50 000 K) torsion angle dynamics (15 ps), followed by 1000 steps of torsion angle dynamics (15 ps) during which the temperature was reduced from 50 000 to 298 K, and 6000 steps of Cartesian dynamics (5 ps) during which the temperature was reduced from 2000 to 298 K. The final scale factors for CNS energy terms were as follows: 150 for NOE, 4 for van der Waals, and 200 for dihedral angle. The force constant for orientational constraints was 0.1. The potential function for all constraints was soft-square. Once the backbone rmsd reached 1.1 Å, hydrogen bond constraints were added where unambiguous donor−acceptor pairs could be identified. A grid search was performed to identify values of the molecular alignment tensor leading to the lowest total energy upon inclusion of the orientational constraints. Only residual dipolar coupling constants for residues in regions of defined secondary structure were incorporated in the refinement. Multiple rounds of structure calculation were performed, leading to a final ensemble of 26 structures with a mean CNS energy of 357 and a backbone rmsd of 0.57 ± 0.08 Å (Table 1). It was necessary to reduce the energetic penalty coefficient for a residual dipolar coupling constant violation

Table 1: Final CNS Energies (kcal/mol) for the NtrC[r] Ensemble

$E_{overall}$	357 ± 24.6	$E_{improper}$	16.0 ± 2.55
E_{noe}	43.4 ± 5.94	E_{vdw}	161 ± 18.6
E_{cdih}	2.4 ± 0.58	E_{coup}	2.40 ± 0.577
E_{bond}	16.3 ± 1.48	E_{sani}	8.57 ± 1.12
E_{angle}	108 ± 6.83		

to 0.1 to achieve good convergence and a low final CNS energy. Higher values resulted in highly unfavorable van der Waals clashes. Despite the low coefficient, the observed residual dipolar coupling constants fit the calculated structures well as determined with the program SSIA (alignment tensor, $D_a = -14.9 \pm 0.4$ Hz, $D_r/D_a = 0.624 \pm 0.08$, rmsd between measured and predicted residual dipolar coupling constants of 4.4 Hz, correlation coefficient of 0.94) (46). A final minimization stage consisting of 10 cycles of 200 steps of minimization was performed using CNS. Inclusion of the beryllofluoride group in the calculations has no measurable effect on the resulting structures (20); therefore, the beryllofluoride–aspartate group was represented by an aspartate. PROCHECK-NMR was used to analyze the quality of the resulting structures, and SSIA was used to check the consistency between the structure and the measured residual dipolar couplings. The program MOLMOL (47) was used to analyze the structures.

Active Site Model. A second ensemble of structures was calculated using the final constraint set from the NMR data as well as additional distance constraints obtained by analysis of the crystal structure of beryllofluoride-activated CheY. The additional constraints were (1) a hydrogen bond from Thr82 Hγ1 (OH) to phosphoryl-Asp54 OP*, (2) a salt bridge from Lys104 Hζ* to phosphoryl-Asp54 OP*, and (3) a hydrogen bond from Lys104 Hζ* to Asp10 Oδ1. A phosphate group in the active site was used for these calculations. The annealing protocol was identical to that described for calculation of the NMR structure using CNS. PROCHECK-NMR was used to analyze the quality of the resulting structures.

Peptide Binding by NtrC[r]. Evidence for peptide–NtrC[r] interaction was obtained by comparison of the ^{15}N–^{1}H HSQC (48) spectrum in the absence of peptide with that in the presence of 0.33, 0.67, 1.0, and 2.0 molar equiv of peptide. Spectral changes consistent with rapid exchange on the NMR time scale were observed for all three wild-type peptides with active NtrC[r], and with the 18-mer S160F peptide. No changes were observed upon addition of the 18-mer to inactive NtrC[r]. Only very small changes were observed upon addition of the 18-mer reverse to NtrC[r]. The combined chemical shift changes for NtrC[r] backbone amides upon addition of the 27-mer were quantitated from HSQC spectra. The dissociation constant for the 27-mer was determined in a titration using 300 μM active NtrC[r] with 10 peptide concentrations between 0.1 and 11.7 mM. The combined chemical shift difference in Hertz for Ser92 relative to unbound NtrC[r] was determined, and the resulting data were fit to a standard isotherm using the program Grace, yielding a dissociation constant of 5.4 mM.

Backbone Dynamics. T_1, T_2, and heteronuclear NOE values were measured at both 500 and 600 MHz. Heteronuclear NOEs were measured using the pulse sequence of Kay *et al.* (49) with a saturation time of 3 s and a total recycle delay of 4.9 s. T_1 and T_2 values were measured using the pulse sequences of Barbato *et al.* (50). T_1 values were measured using nine delays ranging from 10 to 1205 ms at 500 MHz and using 12 delays ranging from 12 to 1055 ms at 600 MHz. T_2 values were measured using six delays ranging from 8 to 250 ms at 500 MHz and using six delays ranging from 29 to 288 ms at 600 MHz. T_1 and T_2 values for each residue as well as error estimates were obtained by Levenberg–Marquardt fits of the decay curves. Curve fits were performed using built-in fitting functions in the program NMRView. Error estimates were calculated at the 90% confidence level from 100 simulations. Errors in peak intensities and heteronuclear NOE values were estimated using the rmsd of the noise in the spectra. The relaxation data were analyzed using the program Modelfree version 4.10 (51). For Modelfree analysis, a minimum error of 3% of the measured R_1, R_2, or heteronuclear NOE value was specified. Model selection was performed using 500 sets of simulated data generated with Modelfree. The relaxation data were then fit using an axial diffusion model; a discussion of possible complications was presented for the phospho-NtrC[r] protein (25). The conclusion that this approach is adequate should be valid for this work as well.

Protonation State of His84. ^{15}N-labeled NtrC[r] was dialyzed against 10 mM ammonium bicarbonate and lyophilized. Four milligrams of the dry protein was redissolved in 5% ^{2}H$_2$O, 4.4 mM BeCl$_2$, 7.2 mM MgCl$_2$, and 29 mM NaF. The sample was adjusted to pH 9.42 by addition of NaOH. The chemical shifts of Hϵ1 and Nϵ2 of His84 were measured by long-range ^{15}N–^{1}H HSQC at seven pH values between 9.4 and 4.9. The combined chemical shift change of the proton and nitrogen, in hertz, measured as a function of pH was fitted to a standard isotherm using the program Grace (Figure 6). The site of protonation was determined by analyzing the coupling patterns in long-range ^{15}N–^{1}H HSQC spectrum (52). Analysis of the cross-peak pattern observed for NtrC[r] indicated that His84 is protonated on Nϵ2.

RESULTS

Resonance Assignments. Sequence-specific backbone and aliphatic side chain assignments were obtained using double- and triple-resonance experiences as described above. Assignments were obtained for all backbone amides except Gln2, Leu65, Leu66, and Lys104, and for 92% of the nonexchangeable side chain protons. Resonance assignments were obtained for the backbone amides of Met60, His84, Ala85, Tyr101, and Phe106, which were not assigned in P-NtrC[r]. Only one backbone amide, Arg56, had chemical shift values that differed significantly from those reported for P-NtrC[r]. The reported shifts for Arg56 in P-NtrC[r] are identical to those reported for inactive NtrC, suggesting that the shifts reported for Arg56 in P-NtrC[r] may have been misreported.

Quality of Structures. A composite Ramachandran plot for the 26 structures in the final ensemble indicates that 97% of the backbone dihedral angles are in allowed and generously allowed regions as determined by the program PROCHECK-NMR (53). Unstructured regions at the N-terminus and C-terminus and in the loops between β3 and α3 and between β4 and α4 largely account for residues in disallowed regions. In regions of defined secondary structure (residues 5–9, 15–24, 39–47, 49–54, 63–72, 77–82, 89–95, 98–102, and

108−120), 95% of the residues lie in the most favored regions and 100% lie within all allowed regions. The structures were defined well by the NOE data, with an average of 9.1 meaningful internuclear distance restraints per residue used in the final structure calculations. Agreement with the NOE data was generally high, with only nine violations of greater than 0.1 Å and no violations of greater than 0.27 Å.

The structures are well-defined, with a backbone heavy atom rmsd of 0.57 ± 0.08 Å for residues 5−120 and an all heavy atom rmsd of 1.03 ± 0.08 Å for the same regions. Importantly, α4 and the loop between β4 and α4, which undergo significant rearrangements upon activation in all receiver domains that have been structurally characterized to date, are defined well by the data; there are an average of 11.2 meaningful restraints per residue for residues 81−96. The packing of helices 3 and 4 against the β-sheet core of NtrC^r, which was not well-defined in the NMR structure of P-NtrC^r, is defined by NOEs between α2 and α3 (a network of contacts between Leu40, Leu43, Lys68, and Ile69), α3 and α4 (NOEs between the methyl groups of Leu63 and the backbone amide of Ala89, between the methyl groups of Ala89 and Ala93, and between HN and Hα of Lys67), α3 to the core (a network of contacts between Ile69 and Leu76 and Val78), and α4 to the core (contacts between the side chain of Tyr101 and Ala90 and Ala93). The contacts between α3 and the core, primarily occurring at the C-terminus of α3, define an orientation of α3 in which the N-terminus of α3 is canted away from the core, and not the C-terminus as was observed in the structure of P-NtrC^r. This difference probably comes from the limited NMR data that were available for P-NtrC^r.

Model Structure Incorporating Active Site Contacts. Side chains of the residues that comprise the active site were not defined well by our NMR data. This is not surprising since many of the interactions which stabilize the local structure in this region are hydrogen bonds and salt bridges which are difficult to identify with NMR. To explore whether conserved residues Asp11, Asp12, and Lys104 could adopt a hydrogen bonding network analogous to the active site conformation observed in the crystal structure of BeF$_3^-$-CheY, an ensemble of structures was calculated using the final restraint set, with the additional active site restraints described in Materials and Methods. The resulting structures remain well-defined, with a backbone rmsd of 0.56 ± 0.08 Å and an all heavy atom rmsd of 0.99 ± 0.09 Å for 26 structures, and are within the structural envelope defined by the BeF$_3^-$−NtrC^r ensemble, with the exception of the loop between β5 and α5, which moves slightly closer to the active site. As expected from the additional constraints, the active site side chains cluster more tightly near the BeF$_3^-$ moiety.

Coordinates for the 26 structures of beryllofluoride-activated NtrC^r with the lowest CNS energies have been deposited in the RCSB Protein Data Bank (entry 1KRW). Coordinates for the 26 structures of the model derived from the NMR constraints and active site arrangement constraints inferred from similarity to CheY have also been deposited in the Protein Data Bank (entry 1KRX). Tables of chemical shifts and constraints have been deposited in the Bio-MagResBank (entry 5278).

Peptide Binding by NtrC^r. Three peptides were prepared spanning the fragment of wild-type NtrC that was predicted

to bind to activated NtrC^r [residues 134−160 (27-mer), 139−160 (22-mer), and 134−160 (18-mer)] and assayed their ability to perturb the ^{15}N−^{1}H HSQC spectrum of berylloflouride-activated NtrC^r. All three peptides produced progressive spectral changes with increasing concentrations, consistent with the formation of rapidly exchanging complexes. The 18-mer peptide produced the largest spectral shifts, although the effects of the 22-mer and 27-mers were similar. Titration of the 18-mer with inactive NtrC^r produced negligible spectral changes that were attributed to small changes in the pH and ionic strength of the sample. Assuming the ability to detect spectral changes as small as 2 Hz, inactive NtrC^r binds the 18-mer at least 20-fold less tightly than berylloflouride-activated NtrC^r. The affinity of the 27-mer peptide for NtrC^r was measured by an NMR titration. Although the solubility of the peptide precluded titration past 70% bound, it was possible to fit the resulting curve to a standard isotherm. The dissociation constant of ≈5 mM so obtained should also be a good estimate for the shorter peptides.

DISCUSSION

Comparison of Berylloflouride-Activated and Phosphorylated NtrC Receiver Domains. The structures of P-NtrC^r [PDB entry 1DC8 (*17*)] and the BeF$_3^-$−NtrC^r complex show similar rearrangements relative to apo-NtrC^r (PDB entries 1DC7 and 1NTR), with the most pronounced changes occurring in α4. Most of the differences between the phospho- and BeF$_3^-$-activated structures are localized in α3 and loops. Although details of α3 and α4 were not defined well by the NMR data for P-NtrC^r, the rotational orientation, overall position, and change in residues involved in α4 in the BeF$_3^-$−NtrC^r complex and P-NtrC^r are quite similar. The position of α3, however, is noticeably different in the two active structures. In P-NtrC^r, the N-terminus of α3, which is marginally defined as a helix in this structure, is canted away from the central β-sheet. In the BeF$_3^-$−NtrC^r complex, the helix axis is roughly parallel to the sheet surface, a conformation more like those observed for CheY, Spo0A^r, and FixJ^r in their activated states. To explore further whether this difference could be real, we measured ^{15}N−^{1}H residual dipolar coupling constants for P-NtrC^r in the presence of 10 mg/mL phage pf1 (the maximum concentration at which a magnetically oriented state could be maintained in the presence of the phosphodonor and buffer salts). The coupling constants fit the BeF$_3^-$−NtrC^r structure that is closest to the mean with an rmsd of 1.7 Hz (alignment tensor, D_a = 1.5 Hz, D_r/D_a = 0.49), while they fit the P-NtrC^r that is closest to the mean with an rmsd of 1.9 Hz (alignment tensor, D_a = 1.2 Hz, D_r/D_a = 0.38), supporting the idea that apparent differences between the P-NtrC^r and BeF$_3^-$−NtrC^r structures are largely a result of the regions that are not well-defined by the NMR data in P-NtrC^r, and that the BeF$_3^-$−NtrC^r structure is in fact the same as the active phosphorylated form.

Overall Structural Change upon Activation by BeF$_3^-$. The NtrC^r−BeF$_3^-$ complex has a (β/α)$_5$ fold, as found in all receiver domains. The family of 26 refined calculated structures is shown in Figure 1. The average minimized structure of the BeF$_3^-$−NtrC^r complex was compared to the average minimized structure of apo-NtrC^r (PDB entry 1DC7). As judged by a difference−distance plot, segments of the
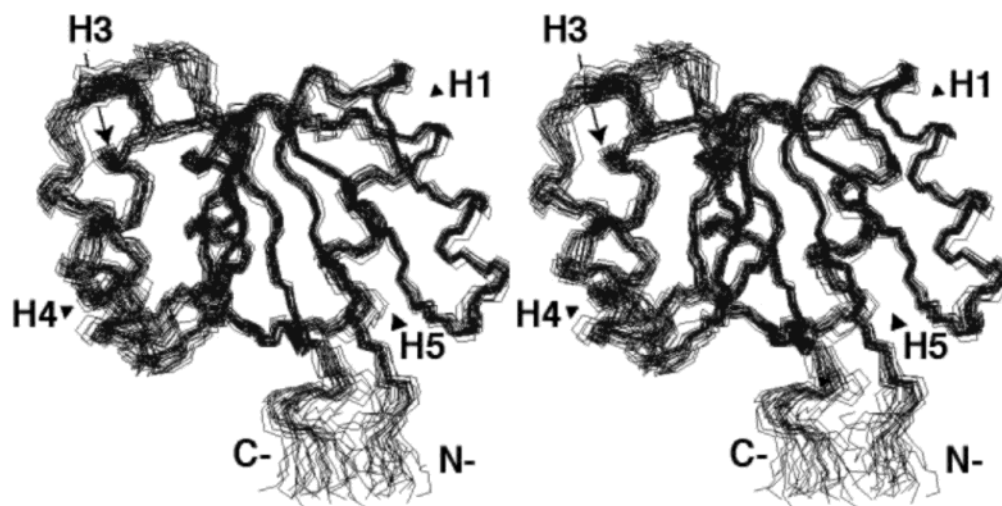
FIGURE 1: Stereoview of the 26 best NMR structures of the BeF_3^-–$NtrC^r$ complex shown with just backbone atoms. The N- and C-termini are indicated, as is the numbering of the helices.

protein that are least affected by activation are made up of residues 4–10, 13–34, 39–55, 63–68, 73–79, 101–105, and 111–122. The active and inactive structures were superimposed using these residues, resulting in $C\alpha$ coordinate differences between these two structures, shown in Figure 2. A sizable structural change (6–9 Å) was observed for residues 83–99, which are located in the $\beta4$–$\alpha4$ loop, $\alpha4$ itself, and the loop between $\alpha4$ and $\beta5$. The structural changes in $NtrC^r$ upon activation are much larger than the changes observed in both CheY and $FixJ^r$ (*16, 21*), also shown in Figure 2. Other regions that exhibit noticeable changes are mostly localized in loops ($\beta1$–$\alpha1$, $\beta2$–$\alpha2$, $\beta3$–$\alpha3$, and $\beta5$–$\alpha5$). The loop between $\beta1$ and $\alpha1$ is known to be involved in Mg^{2+} binding (Asp10 and Asp11). Since the comparison being made is between the apoprotein (no Mg^{2+}) and the active form, the structural change observed in this region is likely due to Mg^{2+} binding rather than phosphorylation or BeF_3^- addition. The remaining loops ($\beta2$–$\alpha2$, $\beta3$–$\alpha3$, and $\beta5$–$\alpha5$) are not well-defined in apo-$NtrC^r$, making it difficult to assess structural changes upon activation. In Figure 3, we show ribbon structures of both apo-$NtrC^r$ and BeF_3^-–$NtrC^r$ complex to visualize the structural changes localized in $\alpha4$ and the loops before and after $\alpha4$.

Detailed Structure Change of the $\beta4$–$\alpha4$ Loop and $\alpha4$: Hydrophobic Core Rearrangement. The structural change in the region of $\alpha4$ was suggested as presenting a new binding surface for interaction with the central ATPase domain (*17*). However, because of the low resolution of the P-$NtrC^r$ structure, it was not possible to define details of side chain interactions between $\alpha4$ and the remainder of the protein, and hence how these two conformers are stabilized. In the structure presented here, the contacts of $\alpha4$ and the loop between $\alpha4$ and $\beta4$, which account for most of the structural changes upon activation, can be characterized in detail. The key interactions involving $\alpha4$ are depicted in Figure 4a. Residues 84–86, which are at the top of the helix in apo-$NtrC^r$, adopt a defined, extended conformation that permits the N-terminus of $\alpha4$ to move away from the central β-sheet; residues 95–97, defined as a loop in apo-$NtrC^r$, become the C-terminus of $\alpha4$ in the BeF_3^-–$NtrC^r$ complex. There is some rotation of $\alpha4$ about its long axis relative to apo-$NtrC^r$, leading to the exposure of the hydrophobic residue Val91
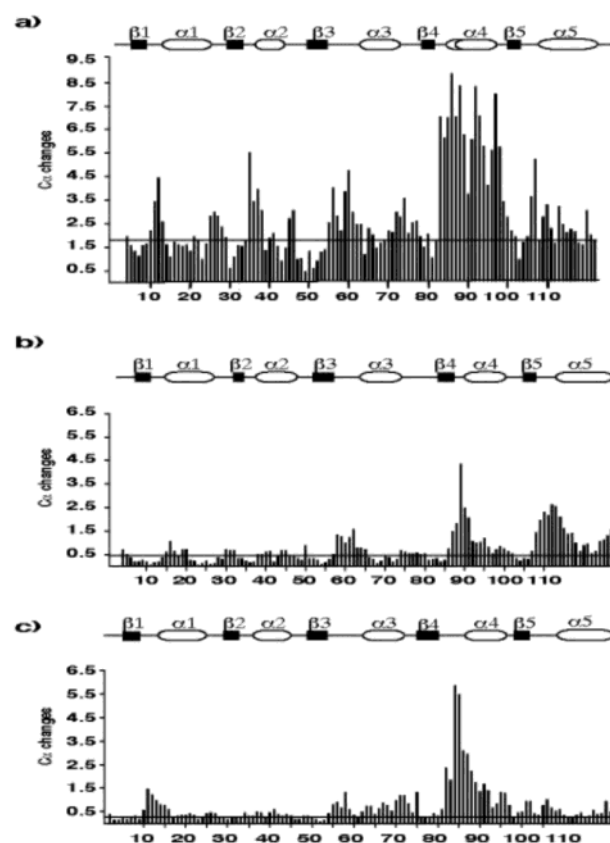

FIGURE 2: Changes in $C\alpha$ coordinate positions upon activation for $NtrC^r$ (a), CheY (b), and $FixJ^r$ (c). For $NtrC^r$, residues 4–10, 13–34, 39–55, 63–68, 73–79, 101–105, and 111–122 were the least influenced by activation and were used to superimpose the apo and BeF_3^--activated forms. For CheY, residues 5–55 and 65–84 were the least influenced by activation and $C\alpha$ positions were used to superimpose Mg^{2+}-bound (PDB entry 2CHE) and BeF_3^--activated (PDB entry 1FQW) forms. For $FixJ^r$, residues least influenced by phosphorylation (residues 1–8, 16–52, and 106–122) were used to superimpose Mn^{2+} (PDB entry 1DCK) and phosphorylated (no metal) (PDB entry 1D5W) $FixJ^r$. The horizontal lines denote the rmsd of superposition of inactive and active structures.

to solvent. Interestingly, three aromatic rings in $\alpha4$ and $\beta5$ exhibited significant movement upon activation: Tyr94, Phe99, and Tyr101 (Figure 4a). The rings of Tyr94 and Phe99 are buried in apo-$NtrC^r$, pointing into the pocket
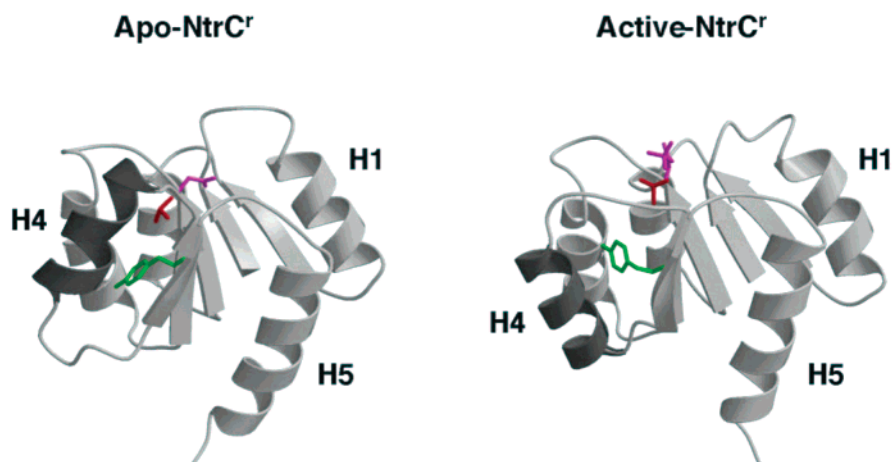
FIGURE 3: Ribbon representations of the apo-NtrC^r (left) and BeF$_3^-$−NtrC^r (right) structures. Side chains of residues Asp54, Thr82, and Tyr101 are shown in magenta, red, and green, respectively. The α4 helix in each structure is shaded dark to emphasize the structural changes that occur upon activation.

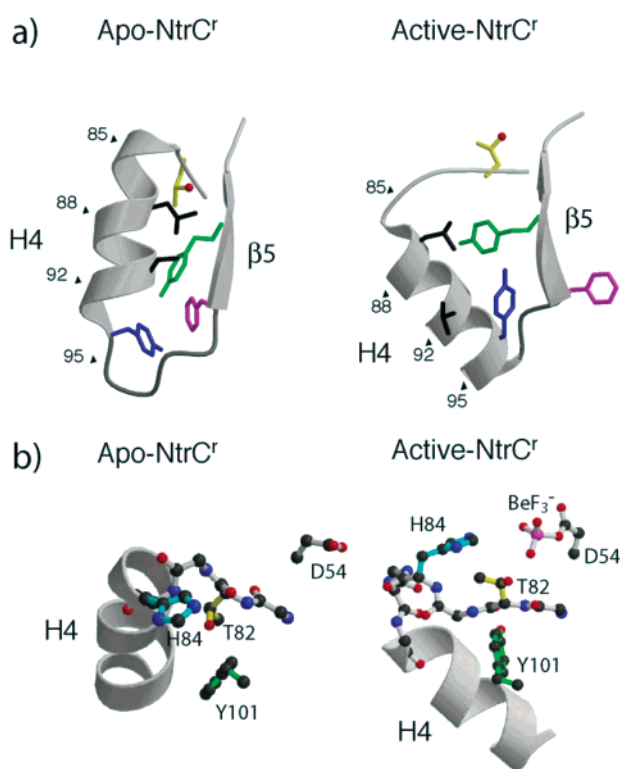FIGURE 4: Details of the activation-induced conformational change in NtrC^r. (a) The hydrophobic core region between β4 and α4 is shown with ribbons (backbone) and sticks (side chain) at key sites: T82 (yellow), L87 (black), V91 (black), Y94 (blue), F99 (blue), and Y101 (green). (b) The loop between β4 and α4 and helix α4 are shown in ball-and-stick and ribbon models, respectively. Key side chains are also shown in ball-and-stick representations, including D54, T82 (yellow), H84 (cyan), and Y101 (green).

between α4 and β5, but are rotated in the BeF$_3^-$−NtrC^r complex. These changes arise from changes in backbone conformation, not just from side chain rotation. The ring of Tyr94 rotates out as a result of this residue's participation in helix formation upon activation. The movement of Phe99 is also due to backbone reorientation as the tilt of β5 is reversed upon activation (Figure 4a). Tyr101 adopts a buried conformation in the BeF$_3^-$−NtrC^r complex. Multiple long-range NOEs orient the aromatic side chain of Tyr101 in the BeF$_3^-$−NtrC^r complex, which adopts consistent χ^1 and χ^2

angles in the ensemble of structures. Although this side chain is also buried in apo-NtrC^r, the orientation differs in the two forms. In the BeF$_3^-$−NtrC^r complex, the aromatic side chain is much closer to the loop between β4 and α4 and is canted differently with respect to the β-sheet core (Figure 4). These ring positions are defined by multiple NOEs in both states. The change of Tyr101 is rather different from that of the equivalent residue in CheY, which moves from a solvent-exposed state in the inactive conformation to a buried one in the active form. This change seems to be the key in modulating the affinity for the downstream target FliM (*22*). The changes in FixJ^r and Spo0A^r upon activation are much closer to those in CheY than those in NtrC^r. It will be interesting to see whether there may be distinct classes of receiver domains according to the rearrangements upon activation.

Proposed Mechanism of Activation: A Novel Coupled Rearrangement of Thr82 and Tyr101. The resolution of the active NtrC^r structure presented here made possible the identification of the side chain interactions described above. In all structures of activated receiver domains which have been described to date, the highly conserved hydroxyl side chain of residue 82 (always Thr or Ser) forms a hydrogen bond with the phosphoryl (beryllofluoride) group at the active site (*15, 16, 21, 22*). As a result of the movement of this residue, a new pocket forms in the interior of the protein and the conserved aromatic side chain of residue 101 (Tyr or Phe) adopts a buried conformation. It is evident from the structure presented above that a similar correlated side chain movement occurs upon beryllofluoride complexation by NtrC^r and, furthermore, that these side chain motions are related to the structural changes that occur in α4. In apo-NtrC^r, the side chain of Thr82 is close to His84, the first residue of α4 in apo-NtrC^r (Figure 4b), and the loop between α4 and β4 (residues 81−84) is compact. Once BeF$_3^-$ (or a phosphoryl group) binds to Asp54, hydrogen bonding between the hydroxyl group of Thr82 and one fluorine (or oxygen in phosphate) stabilizes the geometry of the backbone with Thr82 flipped. With the backbone of Thr82 moved, the N-terminal residues of α4 in apo-NtrC^r (84−86) unwind and take on an extended conformation, which also allows reorientation of the helix. This also makes it possible for two residues (95 and 96) to add to the C-terminus of α4. In

conjunction with this rearrangement, Tyr101 fills the cavity generated by the unwinding of residues 84−86. Thus, the stabilization of Thr82 in a new position leads to a large-scale structural rearrangement of α4 and β5. The reorganization of the side chains of Tyr94 and Phe99 appears to be due to the helical rearrangement and change in position of the Tyr101 ring. Phe99 forms new interactions with α5, but the α5 conformation does not change significantly.

Implications for Binding to the Central ATPase Domain in NtrC and Comparison with Other Response Regulators. As with phosphorylation, beryllofluoride activation of NtrC results in a register shift, displacement relative to the active site, and rotation about the long axis of α4. The rotation of α4 alters the molecular surface by exposing Val91. The position of helix 4 is defined by an extensive network of NOE constraints to residues in both α3 and the β-sheet core (*vide infra*). In both P-NtrC and the BeF_3^-−NtrC complex, α4 lies at an angle with respect to the central β-sheet and is positioned toward the bottom (N-terminal end) of the sheet. The absence of D_{NN} NOEs and observed random-coil chemical shifts are consistent with the extended conformation calculated for residues 84−87, which are helical in apo-NtrC. Additionally, the observed $^{15}N−^1H$ residual dipolar coupling constants imply that the HN−N bond vectors for these residues are not collinear with those in the rest of α4, and backbone dynamics data indicate that Ser85 is extremely mobile (order parameter of 0.1). The structure of the complex of CheY and the N-terminal peptide from its downstream target FliM have shown that N-FliM binds in the pocket between α4 and β5, as well as to the loop between β4 and α4 (*22*). N-Terminal peptides derived from the ATPase domain of NtrC bind in the same pocket as judged by NMR chemical shifts induced by binding. These observations suggest that signaling in NtrC is mediated, at least in part, by conformational changes in α4 and β5, and confirms that the region showing the greatest structural change acts as a binding surface. Ile95 in CheY is involved in formation of the hydrophobic core with the FliM peptide; considering that Val91 in the BeF_3^-−NtrC^r complex is equivalent to Ile95 in BeF_3^--CheY in terms of structure and sequence and becomes exposed to the solvent upon activation, it is probable that Val91 is involved in the interaction with the N-terminal region of the central ATPase domain.

Both NtrC^r and CheY act positively; that is, they interact directly with a downstream partner to affect output. In NtrC, the receiver domain has to bind to the central domain to stimulate assembly of the complex that contacts polymerase and hydrolyzes ATP. In CheY, the rotameric state of Tyr106 seems to determine the signaling state. In the inactive state, Tyr106 is solvent-exposed. In complex with CheA (the histidine kinase in the chemotaxis system), it forms hydrogen bonds to two side chains. In the active state, Tyr106 is buried and forms a hydrogen bond to the backbone of Glu89, stabilizing the active conformation of the β4−α4 loop and better defining the binding surface for FliM. In the Ntr system, NtrB (the histidine kinase) seems to interact with only the receiver domain, and Tyr101 cannot participate directly in the interaction with NtrB since Tyr101 is buried in apo-NtrC^r as well. Instead, Tyr101 probably plays a key role in changing the binding surface to the central domain by filling the cavity that is created by reorientation of α4 and the β4−α4 loop. Thus, instead of a simple switch of

the rotameric state of a single residue observed in CheY, a larger surface changes through a complicated reorganization by way of Y−T coupling in NtrC^r, and this surface change seems to determine the signaling state.

Several features of the active NtrC^r structure reported here, and the structure of apo-NtrC^r reported previously, suggest that while NtrC has many similarities with other members of the response regulator family, there are also significant differences. In particular, α4, which has been implicated in signal output in both NtrC and CheY, lies in a different position and at a different angle to the β-sheet core, and Tyr101 appears to change between buried configurations upon activation, rather than switching from exposed to buried. These features may be related to the intramolecular mode of NtrC regulation, and additional studies on the interaction between the regulatory and ATPase domains of NtrC will be required to further clarify differences.

Peptides Bind the Rearranged Surface of Active NtrC^r. The apparent exposure of hydrophobic residues on the surface of α4 suggested that this region might interact with distal parts of NtrC to enable oligomer formation. From previous work (*54*), there was evidence that the beginning of the central, ATPase domain was the likely contact region. Peptides corresponding to residues 143−160 of NtrC (as well as longer peptides containing this region) do bind to activated NtrC^r (but not to the inactive form), and induce chemical shift changes particularly in the region of α4 (Figure 5). Analogous experiments with CheY and peptides from both FliM and CheZ (*55*) correctly identified the 3445 face of CheY [as verified in subsequently determined structures of each (*22, 56*)] as the site of interaction. The affinity of the NtrC central domain peptides for the activated receiver domain is lower than in the other systems, but the true interaction is intradimer which makes the effective concentration of the target much higher. In addition, it would not be surprising if there were contacts between NtrC^r and other parts of the central domain as well. The chemical shift change profile is somewhat different for NtrC and CheY, but the rather different modes for CheA and FliM/CheZ binding to CheY (*57, 58, 22*) indicate that there can be variation in how a specific protein surface is recognized.

Conformational Fluctuations in NtrC^r. Previously, Nohaile *et al.* (*28*) suggested that regulation of NtrC function was effected allosterically. In this model, constitutive mutations or phosphorylation shifts a preexisting conformational equilibrium between inactive and active conformers toward the active form. This hypothesis was supported by the distribution of constitutively acting mutations throughout the structure, by the ability of constitutive mutations to act concertedly to afford levels of activation greater than those obtained with individual mutations, and by backbone dynamics data for mutant NtrC^r's consistent with a fluctuating structure in the region around α4. According to this model, P-NtrC^r represents one end point of the conformational equilibrium. It is noteworthy that combinations of phosphorylation and constitutive mutations do not lead to levels of transcriptional activation greater than those observed with phosphorylation alone. An important test of both the ability of beryllofluoride complexation to reproduce the structural changes associated with phosphorylation and the allosteric model of NtrC regulation, then, is the ability of beryllofluoride complexation
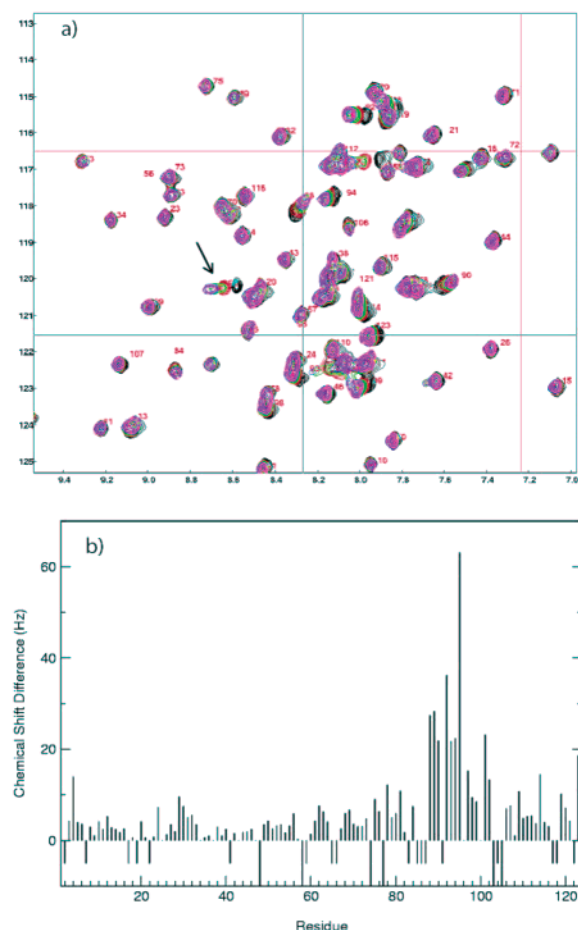
FIGURE 5:   (a) HSQC spectra taken in the course of a titration of the activated NtrC receiver domain with the 27mer peptide from the NtrC central domain (black contours, no peptide; blue, 2 molar equiv). (b) Plot of the chemical shift changes observed in the titration (at 2 molar equiv of peptide per NtrC^r) as a function of position in the sequence of NtrC^r. Values of -10 denote proline residues (which cannot be detected with this approach), and values of -5 denote peaks that could not be assigned, or were overlapped so they could not be reliably followed in the titration.

to convert NtrC to a state that is not measurably interconverting with an associated inactive conformation.

Order parameters for the ^{15}N$-^1$H bond vectors in the $\beta 4-\alpha 4$ loop and $\alpha 4$ of the BeF$_3^-$$-$NtrC^r complex, calculated from T_1, T_2, and heteronuclear NOE measurements at two magnetic fields, indicate that conformational flexibility is confined to Ser85 and possibly Asp86 and Leu87, which could not be measured. The average order parameter of the measured residues in $\alpha 4$ (Ala89, Ala90, Val92, Ser93, and Gln95) was high. Importantly, only nine residues among the 84 residues that were sufficiently well resolved to measure relaxation rates were optimally fit using conformational exchange terms (Val6, Asp11, Ser14, Glu20, Thr29, Val50, Leu63, Ala98, and Asp100). In P-NtrC^r, significant residual conformational exchange was also reported for Leu63 and Asp100 (25). The amide proton of Leu63 is located in $\alpha 3$ and points to the flexible loop between $\beta 3$ and $\alpha 3$, above the active site. Thus, the fact that Leu63 has a conformational exchange term does not necessarily mean that it undergoes a backbone motion. However, it is probable that $\alpha 3$ is still flexible or undergoes conformational exchange since both the Leu65 and Leu66 amide peaks are broadened. Even with this evidence, it is hard to conclude how $\alpha 3$ contributes to
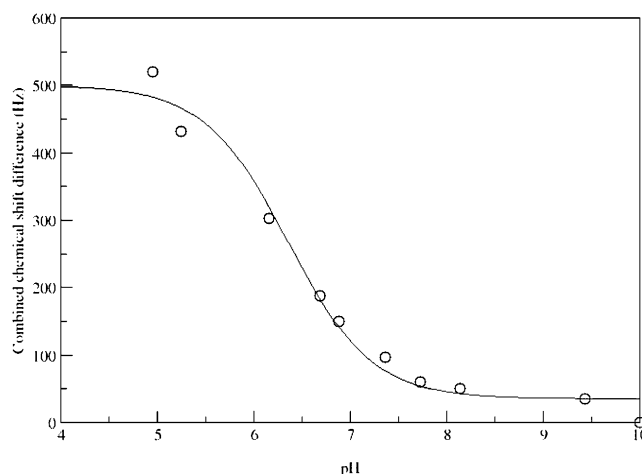
FIGURE 6:   Change in chemical shift of the H84 ring protons as a function of pH. The derived pK value is 6.36.

the activation of NtrC^r since we do not observe a significant structural change in $\alpha 3$ upon activation. The change in exchange broadening in $\alpha 4$ (large in the apo and mutant forms, not detected in the phospho or BeF$_3^-$-activated protein) is the best indication of a preexisting conformational equilibrium because it undergoes a large, distinct structural change between the apo and activated forms.

A Possible Role for His84 in Autodephosphorylation. The position of the His84 side chain is defined to be over the active site by NOEs between His84 H$\delta 2$ and HN and the δ-CH$_3$ group of Ile55 (Figure 4b). In FixJ, His84 is also found in a similar conformation (16). Birck *et al.* (16) suggest that His84 serves to retard dephosphorylation by blocking the entry of water into the active site. We suggest that while this residue could play a steric role in regulating autodephosphorylation, the position of this residue is also consistent with it serving as a base to activate a water molecule positioned immediately above the phosphoryl group for displacement of the phosphate. In this regard, it is interesting to note that the residue at position 83 is highly conserved as Ala or Gly, sterically nondemanding residues, and that receiver domains with long half-lives of the phosphorylated state have conserved residues at position 84 that are unable to act as a general base at physiological pH [for example, Tyr82 in Spo0F (59)]. Moreover, in the BeF$_3^-$$-$CheY crystal structure, the hydroxyl proton of the conserved aromatic residue corresponding to Tyr101 forms a hydrogen bond with the backbone carbonyl of the residue equivalent to His84, potentially stabilizing a functionally important conformation while the protein is in the active state (22). The pK_a of His84 in NtrC^r was measured by analyzing the pH dependence of the chemical shifts of H$\epsilon 1$ and N$\epsilon 2$, and determined to be 6.36 (Figure 6). The average pK_a value for this side chain is 6.8 (60). At low pH, protonation was found to occur on N$\epsilon 2$, which is the atom responsible for activating the water in the putative mechanism proposed above. Further biochemical studies of proteins containing mutations at this site should more directly determine the role of this residue in determining the phosphorylation lifetime.

The studies described here provide details of the conformational rearrangement of the NtrC receiver domain upon activation, which is quite different from all those previously reported, although the trigger for the event, threonine hydrogen bonding to the active site, seems to be the same.

Peptide binding experiments support the interpretation that increased exposure of hydrophobic residues on helix 4 constitutes (at least part) the binding site for parts of the central domain.

ACKNOWLEDGMENT

REFERENCES

1. Stock, A. M., Robinson, V. L., and Goudreau, P. N. (2000) *Annu. Rev. Biochem. 69*, 183−215.
2. Porter, S. C., North, A. K., Wedel, A. B., and Kustu, S. (1993) *Genes Dev. 7*, 2258−2273.
3. Weiss, D. S., Batut, J., Klose, K. E., Keener, J., and Kustu, S. (1991) *Cell 67*, 155−167.
4. Weiss, V., Claverie-Martin, F., and Magasanik, B. (1992) *Proc. Natl. Acad. Sci. U.S.A. 89*, 5088−5092.
5. Barford, D., Hu, S. H., and Johnson, L. N. (1991) *J. Mol. Biol. 218*, 233−260.
6. Canagarajah, B. J., Khokhlatchev, A., Cobb, M. H., and Goldsmith, E. J. (1997) *Cell 90*, 859−869.
7. Hurley, J. H., Dean, A. M., Thorsness, P. E., Koshland, D. E., Jr., and Stroud, R. M. (1990) *J. Biol. Chem. 265*, 3599−3602.
8. Lin, K., Rath, V. L., Dai, S. C., Fletterick, R. J., and Hwang, P. K. (1996) *Science 273*, 1539−1542.
9. Russo, A. A., Jeffrey, P. D., and Pavletich, N. P. (1996) *Nat. Struct. Biol. 3*, 696−700.
10. Hess, J. F., Oosawa, K., Kaplan, N., and Simon, M. I. (1988) *Cell 53*, 79−87.
11. Igo, M. M., Ninfa, A. J., and Silhavy, T. J. (1989) *Genes Dev. 3*, 598−605.
12. Makino, K., Shinagawa, H., Amemura, M., Kawamoto, T., Yamada, M., and Nakata, A. (1989) *J. Mol. Biol. 210*, 551−559.
13. Weiss, V., and Magasanik, B. (1988) *Proc. Natl. Acad. Sci. U.S.A. 85*, 8919−8923.
14. Wright, G. D., Holman, T. R., and Walsh, C. T. (1993) *Biochemistry 32*, 5057−5063.
15. Lewis, R. J., Brannigan, J. A., Muchova, K., Barak, I., and Wilkinson, A. J. (1999) *J. Mol. Biol. 294*, 9−15.
16. Birck, C., Mourey, L., Gouet, P., Fabry, B., Schumacher, J., Rousseau, P., Kahn, D., and Samama, J. P. (1999) *Struct. Folding Des. 7*, 1505−1515.
17. Kern, D., Volkman, B. F., Luginbuhl, P., Nohaile, M. J., Kustu, S., and Wemmer, D. E. (1999) *Nature 402*, 894−898.
18. Lowry, D. F., Roth, A. F., Rupert, P. B., Dahlquist, F. W., Moy, F. J., Domaille, P. J., and Matsumura, P. (1994) *J. Biol. Chem. 269*, 26358−26362.
19. Yan, D., Cho, H. S., Hastings, C. A., Igo, M. M., Lee, S. Y., Pelton, J. G., Stewart, V., Wemmer, D. E., and Kustu, S. (1999) *Proc. Natl. Acad. Sci. U.S.A. 96*, 14789−14794.
20. Cho, H. S., Lee, S. Y., Yan, D., Pan, X., Parkinson, J. S., Kustu, S., Wemmer, D. E., and Pelton, J. G. (2000) *J. Mol. Biol. 297*, 543−551.
21. Lee, S. Y., Cho, H. S., Pelton, J. G., Yan, D., Berry, E. A., and Wemmer, D. E. (2001) *J. Biol. Chem. 276*, 16425−16431.
22. Lee, S. Y., Cho, H. S., Pelton, J. G., Yan, D., Henderson, R. K., King, D. S., Huang, L., Kustu, S., Berry, E. A., and Wemmer, D. E. (2001) *Nat. Struct. Biol. 8*, 52−56.
23. Park, S., Meyer, M., Jones, A. D., Yennawar, H. P., and Nixon, B. T. (2002) *FASEB J.* (in press).
24. Park, S., Zhang, H., Jones, A. D., and Nixon, B. T. (2002) *Biochemistry 41*, 10934−10941.
25. Volkman, B. F., Lipson, D., Wemmer, D. E., and Kern, D. (2001) *Science 291*, 2429−2433.
26. Lee, J., Owens, J. T., Hwang, I., Meares, C., and Kustu, S. (2000) *J. Bacteriol. 182*, 5188−5195.
27. Hwang, I., Thorgeirsson, T., Lee, J., Kustu, S., and Shin, Y. K. (1999) *Proc. Natl. Acad. Sci. U.S.A. 96*, 4880−4885.
28. Nohaile, M., Kern, D., Wemmer, D., Stedman, K., and Kustu, S. (1997) *J. Mol. Biol. 273*, 299−316.
29. Driscoll, P. C., Clore, G. M., Marion, D., Wingfield, P. T., and Gronenborn, A. M. (1990) *Biochemistry 29*, 3542−3556.
30. Live, D. H., Davis, D. G., Agosta, W. C., and Cowburn, D. (1984) *J. Am. Chem. Soc 106*, 1934−1941.
31. Marion, D., Ikura, M., Tschudin, R., and Bax, A. (1989) *J. Magn. Reson. 85*, 393−399.
32. Johnson, B. A., and Blevins, R. A. (1994) *J. Biomol. NMR 4*, 603−614.
33. Grzesiek, S., and Bax, A. (1992) *J. Magn. Reson. 99*, 201−207.
34. Grzesiek, S., and Bax, A. (1992) *J. Am. Chem. Soc. 114*, 6291−6293.
35. Talluri, S., and Wagner, G. (1996) *J. Magn. Reson. 112*, 200−205.
36. Kay, L. E., Xu, G.-Y., Singer, A., Muhandram, D., and Forman-Kay, J. (1993) *J. Magn. Reson. 101*, 333−337.
37. Majumdar, A., and Zuiderweg, E. R. (1993) *J. Magn. Reson. 102*, 242−244.
38. Vuister, G. W., Clore, G. M., Gronenborn, A. M., Powers, R., Garett, D. S., Tschudin, R., and Bax, A. (1993) *J. Magn. Reson. 101*, 210−213.
39. Bax, A., Max, D., and Zax, D. (1992) *J. Am. Chem. Soc. 114*, 6923−6925.
40. Ottiger, M., Delaglio, F., and Bax, A. (1998) *J. Magn. Reson. 131*, 373−378.
41. Hansen, M. R., Mueller, L., and Pardi, A. (1998) *Nat. Struct. Biol. 5*, 1065−1074.
42. Zhang, Y.-Z. (1995) Ph.D. Thesis, Structural Biology and Molecular Biophysics, University of Pennsylvania, Philadelphia, PA.
43. Guntert, P., Mumenthaler, C., and Wuthrich, K. (1997) *J. Mol. Biol. 273*, 283−298.
44. Cornilescu, G., Delaglio, F., and Bax, A. (1999) *J. Biomol. NMR 13*, 289−302.
45. Brunger, A. T., Adams, P. D., Clore, G. M., DeLano, W. L., Gros, P., Grosse-Kunstleve, R. W., Jiang, J. S., Kuszewski, J., Nilges, M., Pannu, N. S., Read, R. J., Rice, L. M., Simonson, T., and Warren, G. L. (1998) *Acta Crystallogr. D54*, 905−921.
46. Zweckstetter, M., and Bax, A. (2000) *J. Am. Chem. Soc. 122*, 3791−3792.
47. Koradi, R., Billeter, M., and Wüthrich, K. (1996) *J. Mol. Graphics 14*, 51−55.
48. Sklenar, V., Piotto, M., Leppik, R., and Saudek, V. (1993) *J. Magn. Reson., Ser. A 102*, 241−245.
49. Kay, L. E., Torchia, D. A., and Bax, A. (1989) *Biochemistry 28*, 8972−8979.
50. Farrow, N. A., Muhandiram, R., Singer, A. U., Pascal, S. M., Kay, C. M., Gish, G., Shoelson, S. E., Pawson, T., Forman-Kay, J. D., and Kay, L. E. (1994) *Biochemistry 33*, 5984−6003.
51. Mandel, A. M., Akke, M., and Palmer, A. G., III (1995) *J. Mol. Biol. 246*, 144−163.
52. Pelton, J. G., Torchia, D. A., Meadow, N. D., and Roseman, S. (1993) *Protein Sci. 2*, 543−558.
53. Laskowski, R. A., Rullmann, J. A., MacArthur, M. W., Kaptein, R., and Thornton, J. M. (1996) *J. Biomol. NMR 8*, 477−486.
54. Lee, J., Owens, J. T., Hwang, I., Meares, C., and Kustu, S. (2000) *J. Bacteriol. 182*, 5188−5195.
55. McEvoy, M. M., Bren, A., Eisenbach, M., and Dahlquist, F. W. (1999) *J. Mol. Biol. 289*, 1423−1433.
56. Zhao, R., Collins, E. J., Bourret, R. B., and Silversmith, R. E. (2002) *Nat. Struct. Biol. 9*, 570−575.
57. Swanson, R. V., Lowry, D. F., Matsumura, P., McEvoy, M. M., Simon, M. I., and Dahlquist, F. W. (1995) *Nat. Struct. Biol. 2*, 905−910.
58. Welch, M., Chinardet, N., Mourey, L., Birck, C., and Samama, J.-P. (1997) *Nat. Struct. Biol. 5*, 25−29.
59. Zapf, J., Madhusudan, M., Grimshaw, C. E., Hoch, J. A., Varughese, K. I., and Whiteley, J. M. (1998) *Biochemistry 37*, 7725−7732.
60. Cantor, C. R., and Schimmel, P. R. (1980) *Biophysical Chemistry, Part I*, W. H. Freeman, San Francisco.